Materials Research. 2020; 23(4): e20200010
DOI: https://doi.org/10.1590/1980-5373-MR-2020-0010

Vat Photopolymerization Additive Manufacturing Resins: Analysis and Case Study[1]

João Fiore Parreira Lovo[a*], ***Italo Leite de Camargo***[a,b], ***Rogério Erbereli***[a],
Mateus Mota Morais[a], ***Carlos Alberto Fortulan***[a]

[a]*Universidade de São Paulo, Departamento de Engenharia Mecânica, Laboratório de Tribologia e Compósitos, Trabalhador São Carlense, 400, São Carlos, SP, Brasil*
[b]*Instituto Federal de Educação, Ciência e Tecnologia de São Paulo – IFSP, Primeiro de Maio, 500, Itaquaquecetuba, SP, Brasil.*

Received: January 10, 2020; Revised: April 29, 2020; Accepted: June 12, 2020

Additive manufacturing processes have been developed over the last decades, especially vat photopolymerization (VP) processes, due to its simplicity and speed. The objective of this paper is to characterize commercial VP resins widely used for technical applications. Thus, test specimens were printed by Digital Light Processing and subjected to tensile, compression, flexural, hardness, and inorganic composition analyses. The resin with the highest resistance and hardness (containing 0.6 vol% of inorganics load) reached 53 MPa in tension, 110 MPa in compression, 79 MPa in bending, and 82.3 Shore D, which is comparable to injected polymers. A case study was made, replacing the injected gears of a reducer by printed ones and comparing the finite element analysis with resin properties. The characterization and case study results encourage the expansion of VP processes in the manufacturing of products in several industries and service sectors, as well as the development of new composite resins.

Keywords: *3D printing, FEM, photopolymerization, DLP.*

1. Introduction

Research has driven huge advances in additive manufacturing (AM) in recent decades. AM currently allows the manufacture of products in various materials (polymers, metals, ceramics, and composites) and geometries that would be unfeasible or even impossible to manufacture by other processes[1-3]. Throughout the development of AM, vat photopolymerization processes have been highlighted. The studies of Kodama[4] and André et al.[5] are important examples of additive manufacturing precursors that employ light-curable resins. Also, it is worth noting that the first commercial AM system available was based on the same principle[6].

According to ISO/ASTM 52900:2015[7:3], vat photopolymerization (VP) is defined as an "[…] additive manufacturing process in which liquid photopolymer in a vat is selectively cured by light-activated polymerization." By using liquid raw material, VP enables micrometric layer manufacturing or even layerless continuous manufacturing[8]. The light patterns applied on the resin are based on a three-dimensional computational drawing of the part, solidifying the layers and creating an object similar to the precursor drawing. Light can be visible or ultraviolet (UV), depending on the characteristics of the resin employed[9,10]. VP is commonly divided in the literature into three types: vector scan (layers are formed by scanning a polymerization point), Digital Light Processing (DLP) or mask projection (layers are formed at once by projecting the section) and two-photon (micrometric pieces formed by 3D scanning of a polymerization point generated at the intersection of two light sources)[1,9].

Furthermore, VP processes can be divided according to the construction direction of the part (layer overlap on the Z-axis). Thus, the methods in which construction occurs from top to bottom (the platform moves downward as the subsequent top layers are formed) are called top-down. In this case, the light source falls on top, and whenever a layer is ready, the platform descends the equivalent of one layer thickness. In this approach, the main issue is that the thickness of the printed layers is not accurate and constant, given the difficulty of the resin to uniformly wet and coat the already printed layers[9,11]. Figure 1 illustrates the mentioned difficulty. Solving this problem may require a complex system dedicated exclusively to coating and spreading new layers.

On the other hand, VP processes are classified as bottom-up when the platform rises the equivalent of one layer thickness whenever a layer is ready, and thereby, construction occurs from bottom to up. In such processes, to create a new layer, there is periodic detachment of the component being manufactured from the bottom of the vat, introducing stresses and deformations into the component. This detachment is particularly disturbing when processing high-viscosity raw material such as ceramic slurry with a high solid load. Besides, the light passes through the transparent

---

[1] This paper was presented in the 10th Brazilian Congress on Manufacturing Engineering, August 2019, São Carlos/SP.

*email: joao.lovo@usp.br

bottom of the vat, generating light scattering[9,11]. Still, such processes show a significant advantage over the top-down method: there is no need for a coating system, which makes the process considerably faster and simpler[1,12]

Improving mechanical strength is a major goal in research related to additive manufacturing[13,14]. Yunus et al.[15] produced specimens of a commercial photocurable resin to test the tensile strength and elastic modulus of printed bodies. Moreover, Gmeiner et al.[16] employed vat photopolymerization to make a bioactive glass that was identified as a possible bone substitute due to its high mechanical strength obtained. Zeng et al.[17] produced Hydroxyapatite scaffolds by VP with adequate compression performance. Furthermore, strain has also been studied, as is the paper of Patel et al.[18], who produced a photopolymer by DLP that can be stretched more than 1000%.

Another critical attribute in mechanical components is the hardness that represents the ability to resist deformation induced by mechanical indentation or abrasion[19]. This property has been studied in several AM processes such as direct energy deposition[20,21], fused deposition modeling[22,23], and vat photopolymerization[19,24]. In this last process, inorganic additives were employed in light-curing resins to improve various properties as their composition strongly influences the mechanical strength of parts. Accordingly, the proper use of inorganic fillers in 3D printing materials has improved printing quality and expanded their application in several markets[20,25,26]. VP processes have evolved so rapidly in recent years, both in equipment and resins, that final product manufacturing became a reality in several areas.

In addition to the development of materials with suitable properties, the mechanical characterization of resins is critical to proper selection. In this manuscript, five commercial resins for VP processes were characterized. Thus, mechanical and composition tests were performed, seeking to relate the properties of resins and their inorganic additives. Moreover, a study case on the gears of a planetary gear train was made. The gear stresses in different load conditions were modeled through finite element analysis and were compared with the resin properties obtained. This comparison can lead to a better understanding of possible failure modes before mechanical testing. Finally, these gears were manufactured by AM and tested in their application.

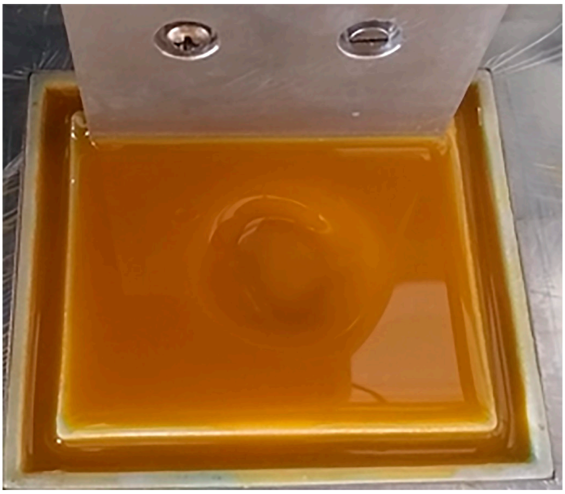

Figure 1. Issue present in top-down VP approach without system dedicated to coating and spreading new layers.

2. Materials and Methods

Vat photopolymerization is characterized by having the best combination of resolution and surface quality among additive manufacturing processes[11,27]. In this paper, five commercial photocurable resins from different manufacturers (Table 1) were evaluated and characterized. All of them are acrylic-based resins whose viscosity varies between 140 and 550 cP (at 25 ± 5 °C), thus being suitable for photopolymerization equipment in general[28]. Hence, the selected resins are widely used in several applications, ranging from dental crowns manufacturing to automotive housings due to the VP ability to print such detailed parts. According to their datasheets, the resins are composed of acrylic monomers and oligomers, photoinitiators, and inorganic additives.

2.1 Additive manufacturing of the specimens

A commercial 3d printer (Hunter, Flashforge Corporation) was used to manufacture specimens and mechanical components. It is a bottom-up DLP equipment (405 nm LED light source) with a printing size of 120 mm x 67.5 mm x 150 mm, resolution of 12.5 µm in the Z-axis (layer height) and 62.5 µm in X and Y axes. The choice of bottom-up equipment was justified by the smaller amount of material required for manufacturing (the printer worked even without the vat being full) and shorter printing time. Thus, this approach allows for reducing costs and waste in the experiments[12,29,30].

The five resins were used to print 50 µm layer thickness samples. The specimens and test parameters for tensile, compressive, and flexural tests followed, respectively, ASTM D638[31], ASTM D695[32], and ASTM D790[33] standards. Consequently, tensile specimens had a width of the reduced section of 3.2 mm and a thickness of 3.2 mm. In the compression tests, cylindrical specimens with a length of 25.4 mm and a diameter of 12.7 mm were used. The flexural specimens were 3.2 mm thick, 12.7 mm wide, and 64 mm long. The built direction of the parts, indicated in Figure 2, was chosen so that the maximum stress during the test occurred perpendicular to the printing layers, thus representing the most critical condition for each test. Finally, for the case study, gears with 18 teeth, 0.5 module, and 4 mm face width were printed with Resin 1 (LS600, EnvisionTEC) for application testing as first stage components in a planetary gear train (3863A024C, Faulhaber GmbH & Co.).

Table 1. Commercial photocurable resins.

RESIN	MANUFACTURER	MODEL
1	EnvisionTEC	LS600
2	Smart Print	Bio Hybrid
3	Smart Dent	Modelo
4	FlashForge	Standard
5	Makertech	DM400

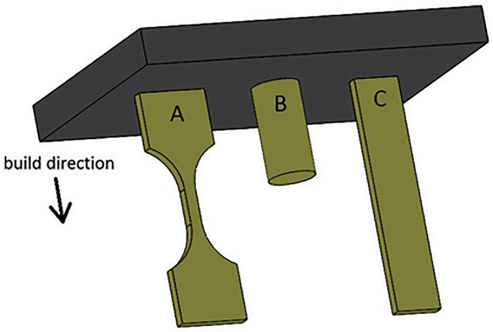

Figure 2. Orientation of specimens printed by vat photopolymerization. (A) Tensile. (B) Compression. (C) Flexural.

2.2 Material characterization

A universal testing machine (Bionix, MTS®) with a load cell of 15 kN was used for the mechanical strength tests. The flexural tests employed a three-point bending device with a 40 mm span. Tensile tests were performed at 1.0 mm/min, while compression and bending tests at 1.5 mm/min. All mechanical tests were carried out at 20 °C. Moreover, Shore D hardness tests were performed on a commercial durometer (Type D2, Shore Instrument & MFG Co INC) with ten indentations in each resin sample, following ASTM D2240[34] guidelines.

Pieces of printed parts were burned in a box furnace (Blue M, Lindberg) at 500ºC for 120 minutes, with a heating rate of 3.5 °C/min, to analyze the inorganic additives present in each resin. For each resin, fragments and their material remaining from burning were weighed on an analytical balance (AUW220D, Shimadzu) with a resolution of 0.01 mg. In order to verify similarities between the inorganic additives and to calculate their volumetric percentage and compare them with the values reported in the literature, the burnt material was analyzed on an X-ray fluorescence spectrometer (EDX 720HS, Shimadzu) under a vacuum atmosphere with a 5 mm collimator aperture. All atomic elements with an atomic number greater than 10 were scanned.

2.3 Case Study and Finite Element Modeling

Resin 1 was chosen for the case study because it presented the best mechanical properties in the tests carried out. This material reached an average ultimate strength superior to the other resins in the tensile, compression, and flexural tests. Resin 1 also presented an average hardness greater than the other materials evaluated in the present paper. Also, a mechanical component, such as a gear, is compatible with the usual application of this resin, unlike some tested resins intended for dental applications.

The finite element analysis of the gear case study was performed with the Abaqus Standard solver. Then, the resulting stresses were compared with the properties obtained in the characterization. The gear tooth profile tooth was designed with a relief radius of 0.2 mm. The following assumptions were made to simplify the analysis and reduce computational cost. First, it was considered that only one pair of teeth would be in contact supporting all the loads at any given time. Therefore, only the gear tooth in contact was simulated (other teeth are unloaded). Second, the simulation was considered in a plane stress condition, with the load equally shared through the thickness of the gear, simplifying the model to a bidimensional analysis. Finally, the problem was considered symmetric because the planetary gear has contact with the sun gear and with the annulus gear with equal force. Therefore, only half of the gear was analyzed. The face width of the gear was 4 mm.

The gear material was modeled as isotropic linear elastic with Young‘s modulus of 3.2 GPa and Poisson‘s ratio 0.3. The linear elastic model was chosen because the stresses developed in the simulation were lower than the linear limit of the material (considering the offset of 0.2% strain). Also, parts printed with the DLP have low anisotropy, due to high layer adhesion and the post-curing process with UV light, minimizing the errors of the isotropic assumption[24]. The following boundary conditions were applied: The vertical displacement and rotation of the nodes of the symmetry line of the gear were constrained. Also, the horizontal displacement of the nodes of the gear hole was constrained.

The gear has two possible failure modes: fracture of the tooth root caused by bending stresses and surface fatigue[35,36]. Each failure mode was analyzed with a different mesh and load condition. About the loads, the catalog of the planetary gearhead (Faulhaber Series 38/1 reduction 66:1) states that the maximum allowed torque is 2200 Nmm. Considering the real reduction ratio of 66.22, the torque in the first gear stage is 33.22 Nmm. The pitch diameter of the sun gear (21 teeth) is 10.5 mm, therefore the tangential force acting in the sun gear is 2.11 N. Finally, the total force applied on the gear was calculated through Equation 1.

$$F = \frac{F_t}{\cos\theta} \tag{1}$$

Where, F is the total force, F_t the tangential force in the pitch diameter, and θ the pressure angle (20°). For the bending analysis, the most critical situation is when the load is applied in the tooth tip, causing the highest bending stress. The line of action of the force formed an angle of 30.28° with the horizontal (Figure 3).

For the surface pressure analysis, the critical condition occurs when the force acts near the pitch diameter. The width of the contact area and the maximum pressure were calculated using the Hertz contact theory for cylinders (Equations 2 and 3)[35].

$$b = \sqrt{\frac{2F\left[\left(\frac{1-\nu_p^2}{E_p}\right)+\left(\frac{1-\nu_g^2}{E_g}\right)\right]}{\pi w\left(\frac{1}{d_p\sin\theta}+\frac{1}{d_g\sin\theta}\right)}} \tag{2}$$

$$p_{max} = \frac{2F}{\pi w b} \tag{3}$$

Where b is contact patch half-width; E_p and E_g are respectively the pinion and gear Young’s modulus; ν_p and ν_g are the pinion and gear Poisson’s ratio; w is the width of the gear (4 mm); d_p and d_g are respectively the pitch diameters of the pinion

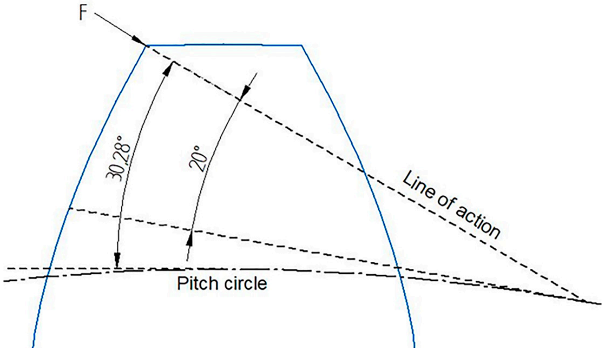

Figure 3. Load applied in the bending condition.

Table 2. Number of elements and nodes of the meshes.

Condition	Mesh	Quadrilateral CPS8 elements	Triangular CPS6 elements	Total number of elements	Total number of nodes
Bending	Coarse	275	19	294	925
Bending	Refined	1853	65	1918	5909
Contact pressure	Coarse	243	23	266	837
Contact pressure	Refined	2107	77	2184	6695

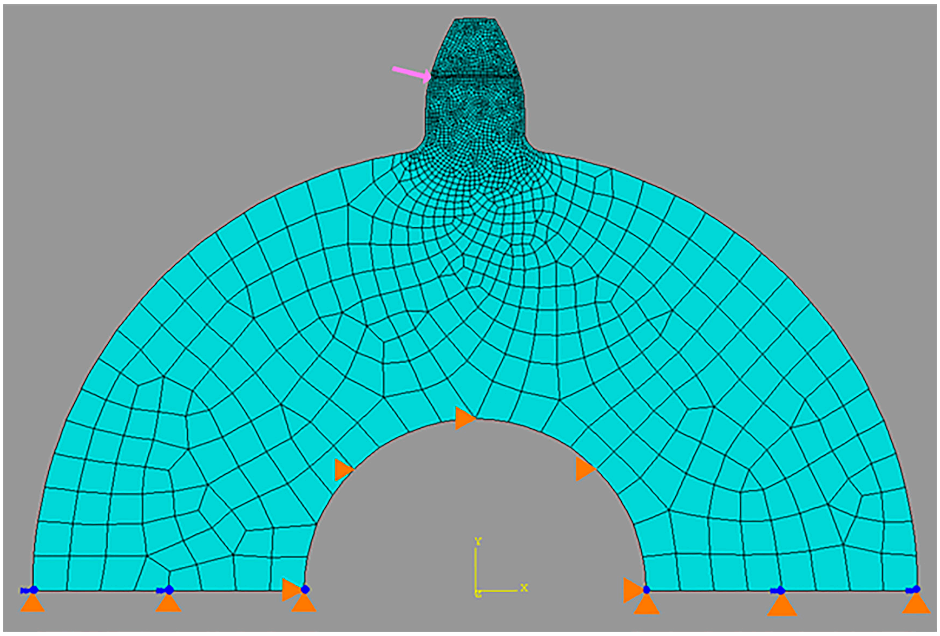

Figure 4. Refined mesh of the contact pressure analysis.

and the gear; p_{max} is the maximum pressure. The maximum pressure of 27.4 MPa was applied in a length of 0.026 mm of the tooth edge considering a uniform distribution (the actual distribution is elliptical, therefore using the maximum pressure is conservative).

Both meshes were built with a quadrilateral (CPS8) and triangular (CPS6) quadratic plane stress elements with full integration. The meshes were automatically generated with free technique, quad dominated, with advancing front. For both conditions, the mesh was more refined on the tooth. In order to evaluate mesh convergence, each condition was simulated with a coarse mesh and a refined mesh. The number of elements and nodes of the meshes is summarized in Table 2. The refined mesh of the contact pressure analysis with the indicative boundary conditions and loads are presented in Figure 4.

The printed gears were assembled on the gear train. Then, the gearbox was positioned on the universal testing machine for static mechanical tests. The reducer housing was fixed to the test machine structure, the output shaft was fixed to the load cell (fixed member), and the input shaft was fixed to the movable member of the testing machine. Then, a torque was applied for 5 minutes to the input shaft in order to generate a continuous 2200 Nmm torque on the output shaft (maximum torque allowed by the planetary gearhead manufacturer). The physical test of the gears reproduced the critical work condition previously tested by FEM, despite not being based on a specific technical standard. Lastly, the reducer was assembled between a stepper motor (NEMA 23) and a LM guide actuator (KR33A, THK) to test the gears in operation.

3. Results and Discussion

The results obtained in the mechanical tests demonstrate a significant difference in the mechanical strength, stiffness, and ductility of the five resins tested. The trends and values observed agree with previous research[37].

3.1 Material Characterization results

In the tensile tests, it was observed wide variation in the resistance, elastic modulus, and maximum elongation in the printed materials. Figure 5 shows the average curves resulting from tensile testing. Resin 1 had the highest tensile strength, reaching an average maximum strength of 53 MPa and modulus of elasticity of 3.0 GPa. Moreover, Resin 2 had the highest elastic modulus among the tested materials (3.2 GPa) and 50 MPa average tensile strength. Such values are equivalent to tensile strength and elastic modulus of high strength polymers manufactured by traditional material injection processes[38,39], demonstrating the feasibility of 3D printing by photopolymerization for the manufacture of high mechanical strength polymers. On the other hand, Resin 5 had the lowest elastic modulus (16 MPa average) and ductility (1.6% maximum strain) among tested resins.

Based on data from the literature, the tensile strength values measured for the five resins tested are within the expected range for 3D printed by vat photopolymerization materials mostly composed of acrylates[40,41]. It was found that the tensile strengths of the tested materials are higher than the value obtained for some materials commonly used in this type of AM, with a formulation based on Poly (ethylene glycol) diacrylate (PEG-DA)[42] and Ethylene glycol phenyl ether acrylate (EGPEA)[41]. Resins 1, 2, and 3 achieved results that place them on the same level as acrylic photopolymers with oligomers and inorganic fillers[15,19]. However, their mechanical strengths are still below those verified in tensile tests with some epoxy materials processed by vat photopolymerization[40].

The tensile tests results also show the low ductility of printed polymers when compared to engineering plastics specimens obtained by traditional manufacturing techniques[36,43]. This relatively low deformation capacity (mainly presented by resins 1, 2, and 5) probably occurs because the printing process is made by layers that favor the propagation of cracks and brittle fractures of the material. However, despite the layered fabrication, the visual analysis of the fracture surfaces of the tested parts does not show that the failures occur by layer detachment, but by crack propagation (transverse to the printing layers), indicating high adhesion between the thin printed layers, as has been observed in other studies[24].

The compression tests also indicated significant variations in the strengths of the tested resins. However, in these tests, all resins achieved a high degree of deformation, exceeding 23% strain before failure. Figure 6 depicts the average curves resulting from the compressive tests. Resin 1 reached the highest strain at failure (greater than 40%) and maximum ultimate compressive strength (110 MPa), while Resin 2 had the highest compressive yield strength (84 MPa). Resins 1, 2, and 3 presented high stiffness (greater than 1.8 GPa). Meanwhile, Resin 5 had the lowest stiffness (1.0 GPa), ultimate (57 MPa), and yield strength (19 MPa) in the compressive test. Furthermore, barreling and abrupt longitudinal fractures were observed in all compressive test specimens.

The average curves resulting from flexural testing (Figure 7) again indicate a wide variation in material strength. In this test, Resin 1 had the highest average maximum strength (79 MPa) and elastic modulus (2.2 GPa), besides having a reasonable deformation capacity before failure, reaching

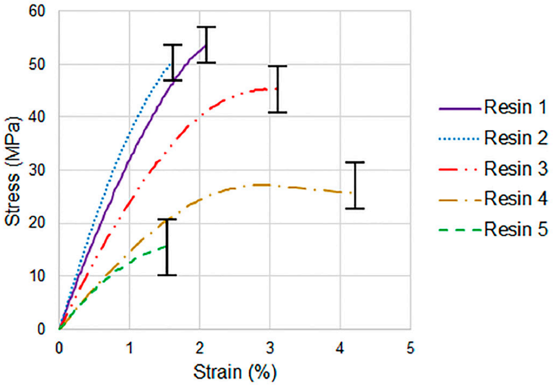

Figure 5. Tensile test results.

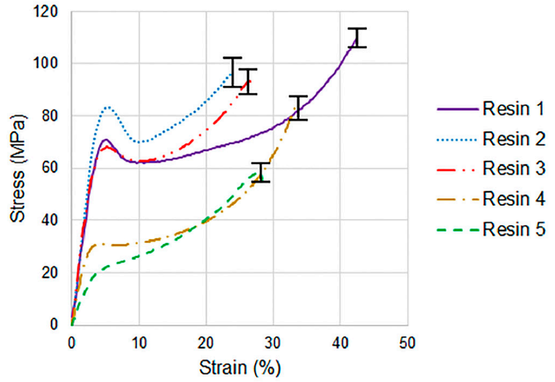

Figure 6. Compressive test results.

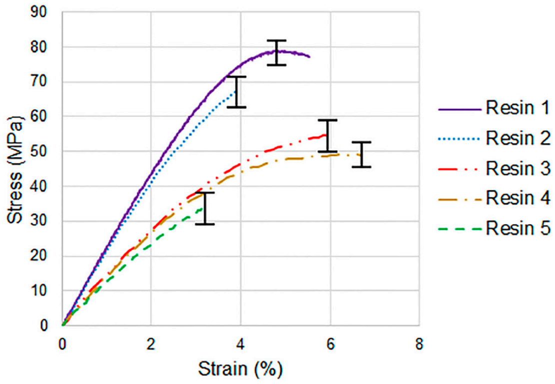

Figure 7. Flexural test results.

maximum strain of 5%. Although Resin 2 also presented good maximum strength (over 65 MPa) for a polymeric material, its maximum strain is less than 4%. Lastly, Resin 5 had the lowest average flexural strength (33 MPa), elastic modulus (1.2 GPa), and strain (about 3.5%). The flexural test results followed the trend and corroborated with the tensile and compressive results since bending is a combination of tensile and compressive stresses in the cross-section where part failure occurs.

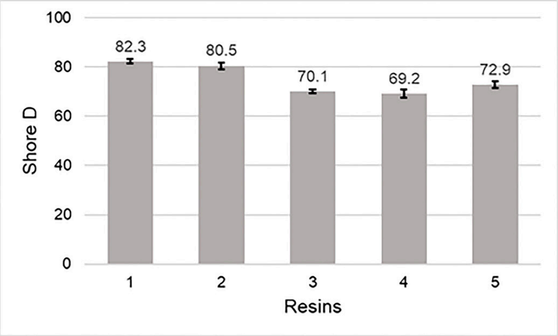

Figure 8. Hardness test results.

Resins 3, 4, and 5 showed flexural strengths compatible with photopolymers based on diacrylates monomers without the addition of reinforcement material[24,44], while Resins 1 and 2 reached strengths equivalent to those of 3D printed specimens with acrylic photopolymer reinforced with inorganic additives[44].

Despite the considerable variation between the resins tested, the results of the tests carried out show that the studied materials have mechanical strength comparable to engineering plastics. For example, the five AM processed photopolymers evaluated in the present paper have tensile[36], compression[38], and flexural[38] strength higher than ordinary injected polyethylene (PE). However, the strengths of the tested resins are lower than the injected polyoxymethylene (POM), tensile[36,38], compressive[36], and flexural strength[38].

Hardness test results are summarized in Figure 8. Resins 1 and 2, which obtained the best compressive properties, also obtained the highest hardness, exceeding 80 Shore D. The lowest average value was obtained by resin 4 (69.2 Shore D). Resins 3 and 5 hardness were respectively 70.1 and 72.9 Shore D.

The measured hardness values for the five materials tested are within the range provided in the literature about

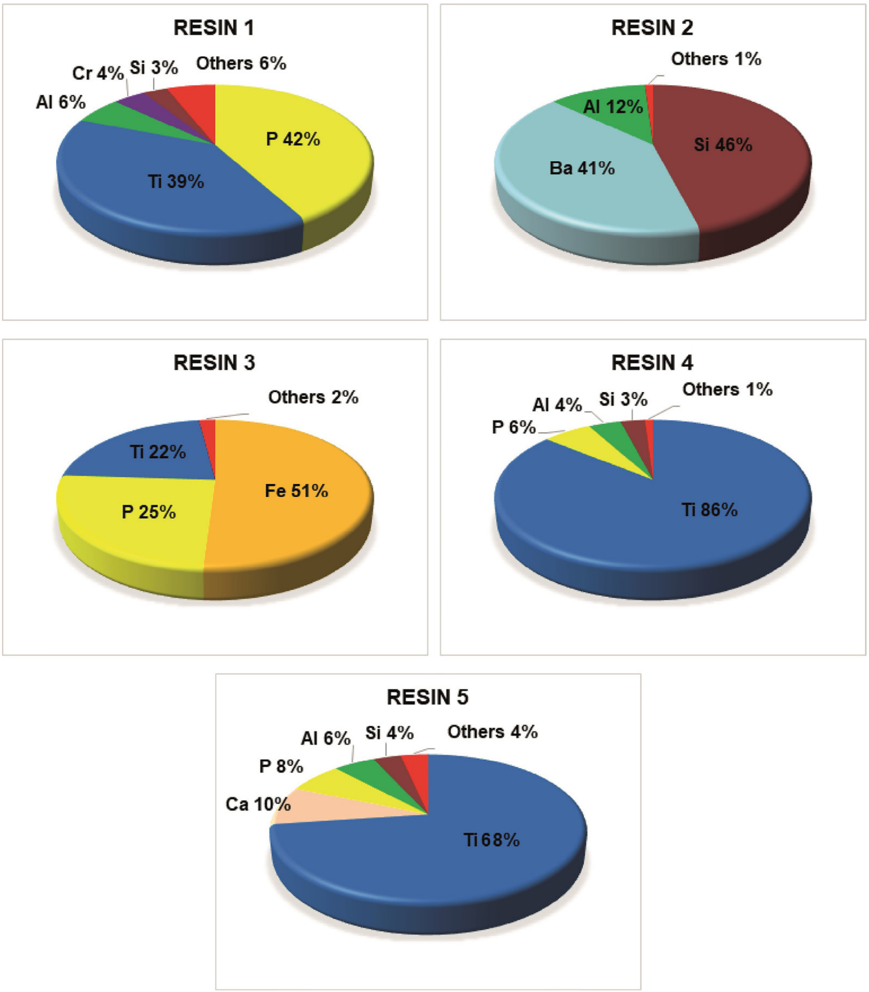

Figure 9. Chemical characterization.

acrylate-based resins processed by vat photopolymerization[19,40]. Also, the hardness test results obtained by Resins 1 and 2, above 80 Shore D, place these materials on the same level as engineering plastics manufactured by traditional material injection processes[38].

Lastly, the results of the chemical composition analysis of the inorganic additives of each of the five resins are shown in Figure 9. Due to the wide variety of chemical compositions of the additives, it was not possible to point out a relationship between the additives used. From the amount of material remaining after burning and their composition, the following load of inorganics was found: 0.6 vol% on Resin 1; 4.1 vol% on Resin 2; 0.8 vol% on Resin 3; 0.1 vol% on Resin 4; and 0.2 vol% on Resin 5. Although the amount of inorganic filler in Resin 2 is very high compared to the other resins analyzed, it is within the quantities of inorganic additives foreseen in the literature to reinforce acrylic-based photopolymers for 3D printing[42,44]. On the other hand, Resins 4 and 5 have a relatively low volume of inorganic additives.

The resin with the largest amount of inorganic additives[2] had the largest tensile elastic modulus, highest compressive yield strength and high hardness and resins with the lowest percentage of inorganic fillers (resins 4 and 5) had the smallest elastic modulus and low hardness. However, it has not been possible to establish a direct relationship between good mechanical properties and a high percentage of additives. Not only the studied fillers had a very different chemical composition, but also some other characteristics can influence mechanical behavior, such as morphology, phase analysis, and functionalization of additives. Future studies may test resins by varying only the percentage of additives to check the correlation between the percentage volume of additives and mechanical properties.

3.2 Case study results

Figure 10 presents the Mises stress on the gear, which was calculated with the finite element method for the bending condition with the refined mesh. As expected, the higher stresses occur in the tooth. The colored contour plot was limited to 7 MPa to highlight the stress field at the tooth root. Figure 11 shows the tooth root in detail.

As can be observed, there are three critical regions: the region where the load was applied, and both fillets at the tooth root. The left fillet is in tension, whereas the right fillet is in compression. The maximum Mises stress caused by bending at the tooth fillet is 6.7 MPa much lower than the materials Yield stress at bending (about 8% of flexural strength). Therefore, the material withstands the static loading. However, because there are two opposite points of contact (one with the solar gear and other with the annular gear), at every revolution, the tooth undergoes an alternate loading cycle. Therefore, material fatigue resistance should also be analyzed. Because the bending stresses are low compared to material yield stress, it is expected that the material would endure a high number of cycles.

Regarding the contact pressure, it was observed that the stresses at the contact area are much higher than in the tooth root. Although the concentrated force is a reasonable hypothesis to evaluate the bending stress at the root, it overestimates the stress at the contact region, resulting in an unrealistic result at the contact point.

A more consistent result was obtained considering the force distributed over a small area at the tooth flank, calculated through the Hertz's contact theory. Figure 12 presents the results of the simulation of the contact pressure condition with the refined mesh.

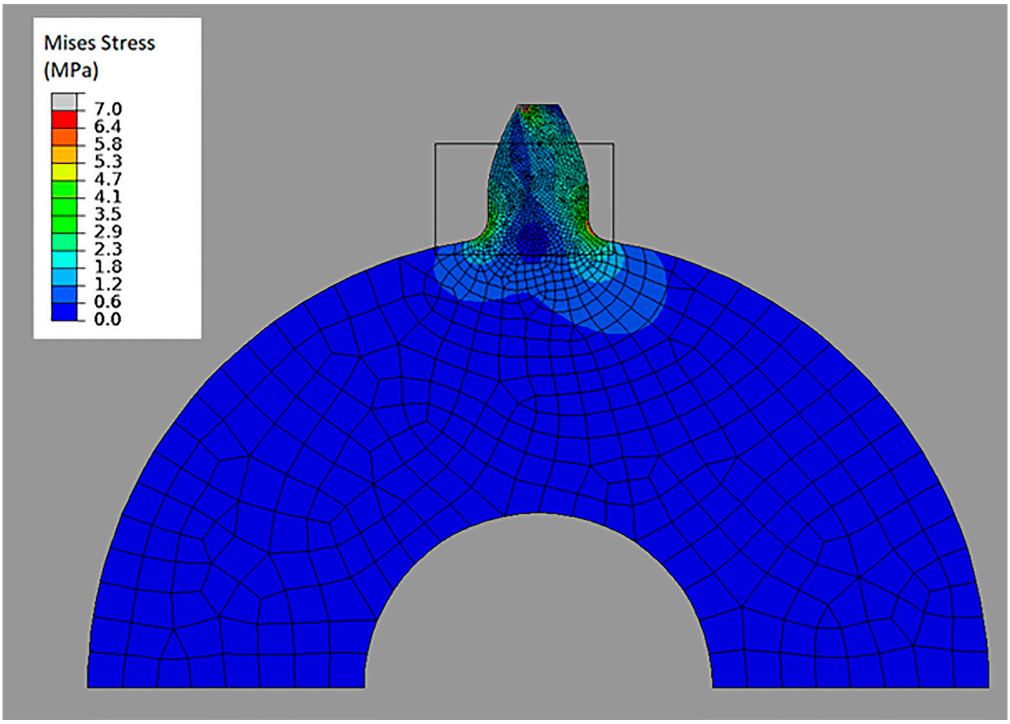

Figure 10. Mises stress field of the bending condition with refined mesh.

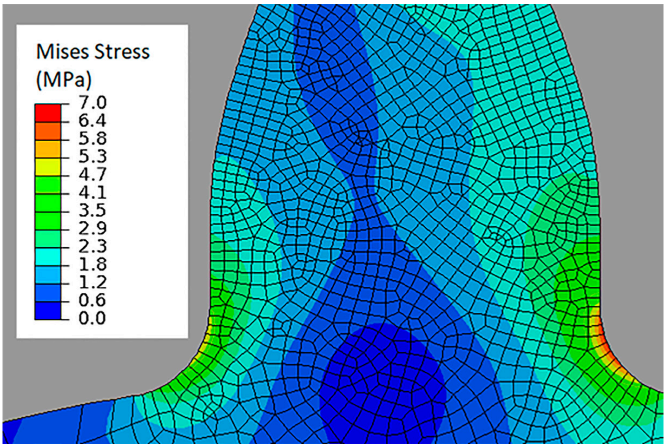

Figure 11. Detail of the stress field at the tooth fillet at the bending condition with refined mesh.

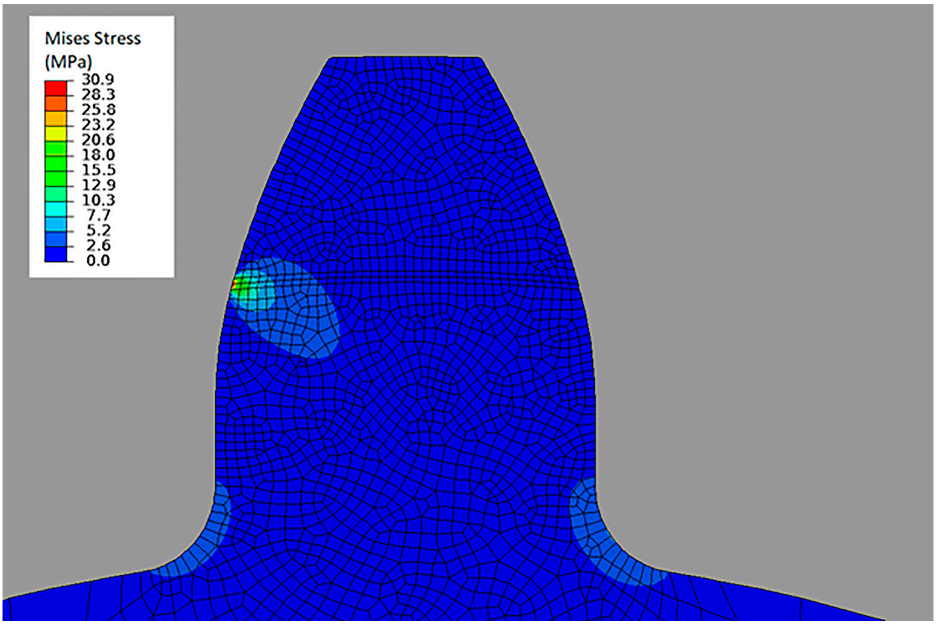

Figure 12. Mises stress field at the tooth at the contact pressure condition with refined mesh.

Table 3. Results of bending and contact pressure analyzes.

Bending analysis		Contact pressure analysis	
Number of nodes	Mises Stress [MPa]	Number of nodes	Mises Stress [MPa]
925	6.9	837	29.8
5909	6.7	6695	30.9

The maximum Mises stress at the contact region was 30.9 MPa (28% of the yield stress in compression). In this condition, the material also withstands the static loading. However, it would probably fail due to fatigue. For this application, surface fatigue is the most probable failure mode because the contact stress is much higher than the bending stress. Up to date, there is no available data for the surface fatigue resistance of the resin used to manufacture the gears. Therefore, it is difficult to predict the service life of the gear without further experiments. Future studies might bring some light regarding the surface service life of additive manufactured gears.

Table 3 summarizes the results. The table highlights the mesh convergence. Refining the mesh six times changed the results by less than 4%. Further refining the mesh would not significantly improve the results and would increase the computational cost unnecessarily.

Thus, the printed gears were assembled on the gear train, as shown in Figure 13. The printed components resisted the static mechanical loading of the application as predicted

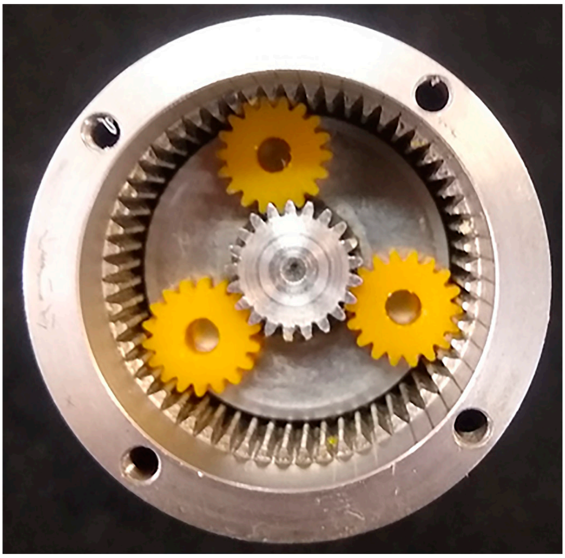

Figure 13. VP printed gears assembled in the reducer.

by finite element analysis. After 5 minutes of continuous load, the printed gears were inspected, and no failure was detected. The reducer with the gears manufactured by VP properly worked when assembled between a stepper motor and a LM guide actuator, with the mechanical system moving without locking.

4. Conclusions

The selected resins characterized in this manuscript presented wide mechanical variation in VP manufactured pieces as a result of the singularity of each formulation. Some of the DLP printed parts showed tensile, compression, and flexural strength, as well as elastic modulus similar to engineering polymers manufactured by the injection molding process. Despite the considerable variation in hardness values, all analyzes resins presented a high performance compared to conventional polymers.

The analysis of inorganic additives of the studied resins revealed considerable variation. The resin with the highest loading (Resin 2) has 40 times more inorganic fillers percentage volume than the resin with the smallest percentage volume of additives (Resin 4). Moreover, the chemical characterization did not allow pointing out similar inorganic additives among the resins analyzed, due to the great variety of chemical compositions of these additives, containing metallic and non-metallic elements. Besides, resins with lower amounts of inorganic fillers were found to be the least resistant and least rigid.

In the case study performed, the printed gears assembled on the first stage of a commercial reducer resisted the application of nominal torque, as predicted in the finite element analysis. Moreover, the gear unit with printed parts properly worked, also highlighting the dimensional quality provided by DLP 3D printing.

This research encourages the expansion of VP processes in the research and manufacturing of products in several industry and service sectors. Furthermore, the results inspire the development of new composite resins with different load volumes of inorganics, chemical composition, morphology, and functionalization of additives.

5. Acknowledgments

This study was financed in part by the Coordenação de Aperfeiçoamento de Pessoal de Nível Superior - Brasil (CAPES) - Finance Code 001.

6. References

1. Gibson I, Rosen D, Stucker B. Additive manufacturing technologies: 3D printing, rapid prototyping, and direct digital manufacturing. 2nd ed. New York: Springer Science; 2015. 498 p.
2. Chiu SH, Gan SY, Tseng YC, Chen KT, Chen CC, Su CH, et al. Multi-objective optimization of process parameters in an area-forming rapid prototyping system using the Taguchi method and a grey relational analysis. Proc Inst Mech Eng, B J Eng Manuf. 2017;231(12):2211-22.
3. Kim H, Lin Y, Tseng TLB. A review on quality control in additive manufacturing. Rapid Prototyping J. 2018;24(3):645-69. https://doi.org/10.1108/RPJ-03-2017-0048.
4. Kodama H. Automatic method for fabricating a three-dimensional plastic model with photo-hardening polymer. Rev Sci Instrum. 1981;52(11):1770-3.
5. André JC, Le Mehauté A, De Witte O, inventors; Compagnie Industriel des Lasers CILAS SA, assignee. Dispositif pour realiser un module de piece industrielle. République Française patent FR 2567668A1. 1984.
6. Hull CW, inventors; Fulwider P, Rieber L, Utecht, assignee. Apparatus for production of three-dimensional objects by stereolithography. United States patent US 4575330. 1986.
7. International Organization for Standardization – ISO. ISO/ASTM 52900:2015(en), Additive manufacturing — General principles — Terminology. Geneva: ISO; 2015.
8. Tumbleston JR, Shirvanyants D, Ermoshkin N, Januszіewicz R, Johnson AR, Kelly D, et al. Continuous liquid interface production of 3D objects. Science. 2015;347(6228):1349-52.
9. Ahrens CH. Processos de AM por fotopolimerização em cuba. In: Volpato N, editor. Manufatura aditiva tecnologias e aplicações da impressão 3D. São Paulo: Editora Blucher; 2017. p. 129-44.
10. Olmos LG, Lovo JFP, De Camargo IL, Consoni CR, Fortulan CA. 3D DLP additive manufacturing: printer and validation. In: 24th ABCM International Congress of Mechanical Engineering; 2017; Curitiba. Proceedings. Rio de Janeiro: ABCM; 2017.
11. Santoliquido O, Colombo P, Ortona A. Additive manufacturing of ceramic components by digital light processing: a comparison between the "bottom-up" and the "top-down" approaches. J Eur Ceram Soc. 2019;39(6):2140-8. https://doi.org/10.1016/j.jeurceramsoc.2019.01.044.
12. Emami MM, Barazandeh F, Yaghmaie F. Scanning-projection based stereolithography: method and structure. Sens Actuators A Phys. 2014;218:116-24. http://dx.doi.org/10.1016/j.sna.2014.08.002.
13. Matsuzaki R, Ueda M, Namiki M, Jeong TK, Asahara H, Horiguchi K, et al. Three-dimensional printing of continuous-fiber composites by in-nozzle impregnation. Science Report. 2016 Feb;6:1-7. http://dx.doi.org/10.1038/srep23058.
14. Gurrala PK, Regalla SP. Multi-objective optimisation of strength and volumetric shrinkage of FDM parts: a multi-objective optimization scheme is used to optimize the strength and volumetric shrinkage of FDM parts considering different process parameters. Virtual Phys Prototyp. 2014;9(2):127-38. http://dx.doi.org/10.1080/17452759.2014.898851.

15. Yunus DE, Shi W, Sohrabi S, Liu Y. Shear induced alignment of short nanofibers in 3D printed polymer composites. Nanotechnology. 2016;27(49):495302.
16. Gmeiner R, Mitteramskogler G, Stampfl J, Boccaccini AR. Stereolithographic ceramic manufacturing of high strength bioactive glass. Int J Appl Ceram Technol. 2015;12(1):38-45.
17. Zeng Y, Yan Y, Yan H, Liu C, Li P, Dong P, et al. 3D printing of hydroxyapatite scaffolds with good mechanical and biocompatible properties by digital light processing. J Mater Sci. 2018;53:6291-301. https://doi.org/10.1007/s10853-018-1992-2.
18. Patel DK, Sakhaei AH, Layani M, Zhang B, Ge Q, Magdassi S. Highly stretchable and UV curable elastomers for digital light processing based 3D printing. Adv Mater. 2017;29(15):1-7.
19. Yang Y, Li L, Zhao J. Mechanical property modeling of photosensitive liquid resin in stereolithography additive manufacturing: bridging degree of cure with tensile strength and hardness. Mater Des. 2019;162:418-28. https://doi.org/10.1016/j.matdes.2018.12.009.
20. Li Y, Hu Y, Cong W, Zhi L, Guo Z. Additive manufacturing of alumina using laser engineered net shaping: effects of deposition variables. Ceram Int. 2017;43(10):7768-75.
21. Niu F, Wu D, Ma G, Wang J, Zhuang J, Jin Z. Rapid fabrication of eutectic ceramic structures by laser engineered net shaping. Procedia CIRP. 2016;42:91-5. http://dx.doi.org/10.1016/j.procir.2016.02.196.
22. Singh S, Singh R. Effect of process parameters on micro hardness of Al-Al2O3 composite prepared using an alternative reinforced pattern in fused deposition modelling assisted investment casting. Robot Comput-Integr Manuf. 2016;37:162-9. http://dx.doi.org/10.1016/j.rcim.2015.09.009.
23. Singh R, Trivedi A, Singh S. Experimental investigation on shore hardness of barrel-finished FDM patterns. Sādhanā. 2017;42(9):1579-84.
24. Monzón M, Ortega Z, Hernández A, Paz R, Ortega F. Anisotropy of photopolymer parts made by digital light processing. Materials (Basel). 2017;10(1):1-15.
25. Park HK, Shin M, Kim B, Park JW, Lee H. A visible light-curable yet visible wavelength-transparent resin for stereolithography 3D printing. NPG Asia Mater. 2018;10(4):82-9. http://dx.doi.org/10.1038/s41427-018-0021-x.
26. Johansson E, Lidström O, Johansson J, Lyckfeldt O, Adolfsson E. Influence of resin composition on the defect formation in alumina manufactured by stereolithography. Materials (Basel). 2017;10(2):1-12.
27. Layani M, Wang X, Magdassi S. Novel materials for 3D printing by photopolymerization. Adv Mater. 2018;30(41):1-7.
28. Bártolo PJ. Stereolithography - materials, processes and applications. USA: Springer; 2011.
29. Lian Q, Yang F, Xin H, Li D. Oxygen-controlled bottom-up mask-projection stereolithography for ceramic 3D printing. Ceram Int. 2017;43(17):14956-61. http://dx.doi.org/10.1016/j.ceramint.2017.08.014.
30. Varghese G, Moral M, Castro-García M, López-López JJ, Marín-Rueda JR, Yagüe-Alcaraz V, et al. Fabricación y caracterización de cerámicas medinate impresión 3D DLP de bajo coste. Bol Soc Esp Ceram Vidr. 2018;57(1):9-18. http://dx.doi.org/10.1016/j.bsecv.2017.09.004.
31. ASTM International. ASTM D638-14, Standard Test Method for Tensile Properties of Plastics. West Conshohocken: ASTM International; 2014.
32. ASTM International. ASTM D695-15, Standard Test Method for Compressive Properties of Rigid Plastics. West Conshohocken: ASTM International; 2015.
33. ASTM International. ASTM D790-17, Standard Test Methods for Flexural Properties of Unreinforced and Reinforced Plastics and Electrical Insulating Materials. West Conshohocken: ASTM International; 2017.
34. ASTM International. ASTM D2240-15, Standard Test Method for Rubber Property—Durometer Hardness. West Conshohocken: ASTM International; 2015.
35. Budynas RG, Nisbett JK. Shigley's mechanical engineering design. 10th ed. New York: McGraw-Hill Education; 2014.
36. Norton RL. Machine design an integrated approach. 3rd ed. Nova Jersey: Prentice Hall; 2006.
37. Lovo JFP, Masalskas EC, Kimura RN, Elui VMC, Fortulan CA. Análise de resinas para manufatura aditiva por DLP. In: 10º Congresso Brasileiro de Engenharia de Fabricação; 2019; São Carlos. Proceedings. Rio de Janeiro: ABCM; 2019.
38. Ashby M. Materials selection in mechanical design. 3rd ed. Butterworth-Heinemann; 2004.
39. Cruz Sanchez FA, Boudaoud H, Hoppe S, Camargo M. Polymer recycling in an open-source additive manufacturing context: mechanical issues. Addit Manuf. 2017;17:87-105. https://doi.org/10.1016/j.addma.2017.05.013.
40. Medellin A, Du W, Miao G, Zou J, Pei Z, Ma C. Vat photopolymerization 3d printing of nanocomposites: a literature review. J Micro Nano-Manufacturing. 2019;7(3):031006.
41. Borrello J, Nasser P, Iatridis JC, Costa KD. 3D printing a mechanically-tunable acrylate resin on a commercial DLP-SLA printer. Addit Manuf. 2018 Aug;23:374-80. https://doi.org/10.1016/j.addma.2018.08.019.
42. Li VCF, Kuang X, Mulyadi A, Hamel CM, Deng Y, Qi HJ. 3D printed cellulose nanocrystal composites through digital light processing. Cellulose. 2019;26(6):3973-85.
43. Callister WD Jr, Rethwisch DG. Materials science and engineering: an introduction. 9th ed. Hoboken: John Wiley & Sons; 2013.
44. Han Y, Wang FK, Wang H, Jiao X, Chen D. High-strength boehmite-acrylate composites for 3D printing: reinforced filler-matrix interactions. Compos Sci Technol. 2018;154:104-9. https://doi.org/10.1016/j.compscitech.2017.10.026.